Plasmon filters and resonators in metal-insulator-metal waveguides

P. Neutens,[1,2,*] L. Lagae,[1,2] G. Borghs,[1,2] and P. Van Dorpe[1]

[1]*Functional Nano Systems group, IMEC, Kapeldreef 75, B-3001 Leuven, Belgium*
[2]*Laboratory of Solid-State Physics and Magnetism, K.U. Leuven, Celestijnenlaan 200D, B-3001 Leuven, Belgium*

[*]*Pieter.Neutens@imec.be*

Abstract: We present the numerical and experimental demonstration of plasmonic Bragg filters and resonators inside metal-insulator-metal (MIM) waveguides. The presented filters and resonators are fabricated using standard top down lithography methods. The optical bandgap of the integrated Bragg filters is experimentally observed and its optical properties are investigated as a function of the grating pitch and the number of grating periods. Transmission filters based on a nanocavity resonance were measured, obtaining Q-factors above 30. Tuning of the cavity wavelength was experimentally achieved by varying the cavity length.

OCIS codes: (240.6680) Surface plasmons; (250.5403) Plasmonics; (230.7370) Waveguides; (130.3120) Integrated optics devices.

References and links

1. A. Boltasseva, T. Nikolajsen, K. Leosson, K. Kjaer, M. S. Larsen, and S. I. Bozhevolnyi, "Integrated optical components utilizing long-range surface plasmon polaritons," J. Lightwave Technol. **23**(1), 413–422 (2005).
2. P. Berini, R. Charbonneau, N. Lahoud, and G. Mattiussi, "Characterization of long-range surface-plasmon-polariton waveguides," J. Appl. Phys. **98**, 043109 (2005).
3. S. I. Bozhevolnyi, V. S. Volkov, E. Devaux, and T. Ebbesen, "Channel plasmon-polariton guiding by subwavelength metal grooves," Phys. Rev. Lett. **95**, 046802 (2005).
4. E. Moreno, S. G. Rodrigo, S. I. Bozhevolnyi, L. Martin-Moreno, and F. J. Garcia-Vidal, "Guiding and focusing of electromagnetic fields with wedge plasmon polaritons," Phys. Rev. Lett. **100**, 023901 (2008).
5. S. A. Maier, P. G. Kik, H. A. Atwater, S. Meltzer, E. Harel, B. E. Koel, and A. G. Requicha, "Local detection of electromagnetic energy transport below the diffraction limit in metal nanoparticle plasmon waveguides," Nat. Mater. **2**, 229–232 (2003).
6. A. L. Falk, F. L. Koppens, C. L. Yu, K. Kang, N. de Leon Snapp, A. V. Akimov, M. Jo, M. D. lukin, and H. Park, "Near-field electical detection of optical plasmons and single-plasmon sources," Nat. Phys. **5**, 475–479 (2009).
7. R. F. Oulton, V. J. Sorger, D. A. Genov, D. F. P. Pile, and X. Zhang, "A hybrid plasmonic waveguide for subwavelength confinement and long-range propagation," Nat. Photonics **2**, 496–500 (2008).
8. J. A. Dionne, H. J. Lezec, and H. A. Atwater, "Highly confined photon transport in subwavelength metallic slot waveguides," Nano Lett. **6**, 1928–1932 (2006).
9. P. Neutens, P. Van Dorpe, L. Lagae, and G. Borghs, "Electrical excitation of confined surface plasmon polaritons in metallic slot waveguides," Nano Lett. **10,** 1429–1432 (2010).
10. P. Neutens, P. Van Dorpe, I. De Vlaminck, L. Lagae, and G. Borghs, "Electrical detection of confined gap plasmons in metal-insulator-metal waveguides," Nat. Photonics **3,** 283–286 (2009).
11. J. S. Foresi, P. R. Villeneuve, J. Ferrera, E. R. Thoen, G. Steinmeyer, S. Fan, J. D. Joannopoulos, L. C. Kimerling, H. I. Smith, and E. P. Ippen, "Photonic-bandgap microcavities in optical waveguides," Nature **390,** 143–145 (1997).
12. A. R. Md Zain, N. P. Johnson, M. Sorel, and M. De La Rue, "Ultra high quality factor one dimensional photonic crystal/photonic wire micro-cavities in silicon-on-insulator (SOI)," Opt. Express **16,** 12084–112089 (2008).
13. J. Chan, M. Eichenfield, R. Camacho, and O. Painter, "Optical and mechanical design of a "zipper" photonic crystal optomechanical cavity," Opt. Express **17,** 3802–3817 (2009).

#156822 - $15.00 USD Received 19 Oct 2011; revised 2 Dec 2011; accepted 2 Dec 2011; published 30 Jan 2012

14. A. Hosseini, and Y. Massoud, "A low-loss metal-insulator-metal plasmonic Bragg reflector," Opt. Express **14,** 11318–11323 (2006).
15. J.-Q. Liu, L.-L. Wang, M.-D. He, W.-Q. Huang, D. Wang, B. S. Zou, and S. Wen, "A wide bandgap plasmonic Bragg reflector," Opt. Express **16,** 4888–4894 (2008).
16. Y. Liu, Y. Liu, and J. Kim, "Characteristics of plasmonic Bragg reflectors with insulator width modulated in sawtooth profiles," Opt. Express **18,** 11589–11598 (2010).
17. Z. Han, E. Forsberg, and S. He, "Surface plasmon Bragg gratings formed in metal-insulator-metal waveguides," IEEE Photonics Technol. Lett. **19**, 91–93 (2007).
18. Y. Q. D. Gan, J. Ma, J. Cui, C. Wang, and X. Luo, "Spectrally selective splitters with metal-dielectric-metal surface plasmon waveguides," Appl. Phys. B **95,** 807–812 (2009).
19. www.comsol.com.
20. E. D. Palik, *Handbook of Optical Constants of Solids* (Academic Press, New York, 1985).
21. J. A. Sánchez-Gil, "Distributed feedback gratings for surface-plasmon polaritons based on metal nanogroove/ridge arrays," Opt. Lett. **32**(16), 2330–2332 (2007).
22. J. A. Sánchez-Gil, and A. A. Maradudin, "Surface-plasmon polariton scattering from a finite array of nanogrooves/ridges: Efficient mirrors," Appl. Phys. Lett. **86**, 251106 (2005).
23. V. S. Volkov, S. I. Bozhevolnyi, E. Devaux, J.-Y. Laluet, and T. W. Ebbesen, "Wavelength selective nanophotonic components utilizing channel plasmon polaritons," Nano Lett. **7**(4), 880-884 (2007).
24. M. Kuttge, H. Kurz, J. Gómez Rivas, J. A. Sánchez-Gil, and P. Haring Bolívar, "Analysis of the propagation of terahertz surface plasmon polaritons on semiconductor groove gratings," J. Appl. Phys. **101**, 023707 (2007).
25. B. Wang, and G. P. Wang, "Plasmon Bragg reflectors and nanocavities on flat metallic surfaces," Appl. Phys. Lett. **87**, 013107 (2005).
26. B. Min, E. Ostby, V. Sorger, E. Ulin-Avila, L. Yang, X. Zhang, and K. Vahala, "High-Q surface-plasmon-polariton whispering-galery microcavity," Nature **457**, 455–459 (2009).
27. P. A. George, C. Manolatou, F. Rana, A. L. Bingham, and D. R. Grischkowsky, "Integrated waveguide-coupled terahertz microcavity resonators," Appl. Phys. Lett. **91**, 191122 (2007).
28. J.-C. Weeber, A. Bouhelier, G. Colas des Francs, L. Markey, and A. Dereux, "Submicrometer in-plane integrated Surface plasmon cavities," Nano Lett. **7**(5), 1352–1359 (2007).
29. Z. Han, "Ultracompact plasmonic racetrack resonators in metal-insulator-metal waveguides," Photonic Nanostruct. **8**(3), 172–176 (2010).
30. J. Liu, G. Fang, H. Zhao, Y. Zhang, and S. Liu, "Plasmon flow control at gap waveguide junctions using square ring resonators," J. Phys. D Appl. Phys. **43**, 055103 (2010).
31. H. Lu, X. Liu, D. Mao, L. Wang, and Y. Gong, "Tunable band-pass plasmonic waveguide filters with nanodisk resonators," Opt. Express **18**(17), 17922–17927 (2010).
32. W. Cai, J. S. White, and M. L. Brongersma, "Compact, high-speed and power-efficient electrooptic plasmonic modulators," Nano Lett. **9**(12), 4403–4411 (2009).
33. A. Noual, Y. Pennec, A. Akjouj, B. Djafari-Rouhani, and L. Dobrzynski, "Nanoscale plasmon waveguide including cavity resonator," J. Phys.- Condens. Mat. **21**, 375301 (2009).

1. Introduction

Plasmonic waveguides have been studied extensively in the last decade. Fast, low-loss signal transmission has been achieved in long-range surface plasmon polariton waveguides [1, 2]. Also deep subwavelength plasmonic waveguides with a shorter propagation length have been demonstrated [3–10]. In order to modify and tune the transmission spectrum through plasmonic waveguides, waveguide-integrated passive components have to be developed. For instance, high Q-factor band-pass filters can be useful to filter a transmitted signal into different spectral bands in order to realize wavelength division multiplexing. Also passive filters can be applied for routing SPPs through a circuit of waveguides. Passive filters can play an important role for sensing applications too, for example sharp plasmonic notch filters are useful for a future development of a surface-enhanced Raman scattering setup on chip.

In silicon photonics, photonic bandgap microcavities are known to have a resonance with a very high quality-factor going up to 10^8 [11–13]. However, if one transfers this concept from a very low-loss dielectric waveguide to a high-confinement metallic waveguide, losses increase dramatically due to the field penetration inside the metal layers, causing high ohmic losses. Therefore, designing integrated high-quality-factor plasmonic resonators inside subwavelength waveguides is not obvious.

#156822 - $15.00 USD Received 19 Oct 2011; revised 2 Dec 2011; accepted 2 Dec 2011; published 30 Jan 2012

We chose to integrate the passive filters in MIM waveguides due to the good field confinement [8]. To obtain a high-quality resonance for band-pass filters inside a MIM waveguide, the application of microcavities inside plasmonic Bragg reflectors was briefly studied numerically in previous papers [14–16]. However very little work has been published on the experimental realization of this kind of reflectors and resonators. Here a single cavity was inserted inside two plasmonic Bragg reflectors, leading to a resonance with an energy lying inside the photonic bandgap.

First, the properties of integrated Bragg reflectors are studied numerically and experimentally in order to assess the optical properties of the Bragg filter. If a cavity is introduced inside the Bragg grating, a waveguide-integrated resonator is created. By performing FDTD simulations, we will predict the spectral position and quality-factor of the cavity resonance. Also the dependence of the transmitted power through the filter on the geometrical parameters is investigated and optimized. The structures are experimentally studied and the transmission spectra are compared to the simulated results. Finally, we also present a novel approach to reduce the size of integrated plasmonic filters, which is important in high-confinement plasmonic waveguides in order to reduce the resistive losses in the cavity. By replacing the micron-size Bragg mirrors by a thin metal barrier, we demonstrate a filter which can be fabricated on the nanoscale in 3 dimensions.

2. Plasmonic waveguide-integrated Bragg mirrors as band-stop filters

2.1. Theoretical description of Bragg filters

Bragg reflectors or Bragg mirrors are an essential component of photonic devices today. Bragg reflectors based on MIM waveguides have been demonstrated recently. The modulation is achieved by varying the dielectric thickness, which was already studied numerically [17, 18]. Physically, in these waveguides the alternative variation in the thickness leads to periodic modulation of the mode index. For example, for a 100 nm thick SiO_2 core symmetrically surrounded by two semi-infinite gold cladding layers, the mode index equals 1.84 at a free space wavelength of 800 nm. When the core thickness is decreased to 60 nm, the mode index rises to 2.06. This modal index difference is the key point to design these Bragg reflectors inside MIM waveguides. The Bragg wavelength corresponds to the central wavelength of the stop-band and can be formulated by the Bragg condition as was calculated by hosseini et al. [14]

$$d_1 n_{eff,1} + d_2 n_{eff,2} = \frac{\lambda_b}{2} \tag{1}$$

where λ_b, d_1, d_2, $n_{eff,1}$ and $n_{eff,2}$ are respectively the Bragg wavelength and the lengths and effective indices of the waveguide within one period. As a consequence, in this system the center wavelength of the stop-band is determined by both the length and the depth of the indents and protrusions making up the grating inside the waveguide. Another important parameter of the band-stop filter the spectral width of the stop-band. In previously published work on integrated Bragg mirrors [18], the width of the stop-band was approximated to be

$$\Delta w_g = \omega_c \frac{4}{\pi} sin^{-1} \frac{n_{eff,2} - n_{eff,1}}{n_{eff,2} + n_{eff,1}} \tag{2}$$

where ω_c is the central frequency of the stop-band. A variation in the grating's etching depth is reflected in changes in the mode index and hence the Bragg stop-band width. From Eq. (2) it can be inferred that the width of the stop-band is dependent on the difference between the two mode indices and hence a larger stop-band width is observed for a deeper grating etch.

#156822 - $15.00 USD Received 19 Oct 2011; revised 2 Dec 2011; accepted 2 Dec 2011; published 30 Jan 2012

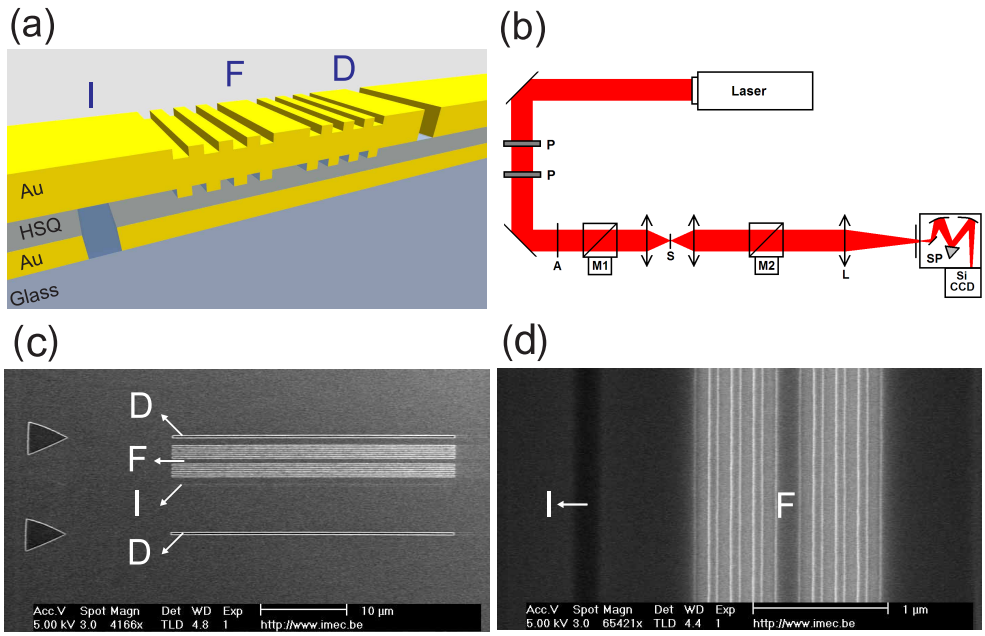

Fig. 1. **(a)** Schematic representation of the waveguide-integrated plasmonic crystal resonator. **(b)** Schematic representation of the transmission setup. **(c)** Top-view scanning electron microscope photograph of a single plasmonic crystal filter. The injection slit, detection slit and filter are indicated with respectively I, D and F. **(d)** Zoom-in on the filter region before the deposition of the top gold layer.

2.2. Fabrication of integrated Bragg filters

For the filter design presented in this report, we choose a Bragg mirror which can be fabricated by one electron beam lithography step followed by a dry etch step. A schematic representation of the investigated structure can be found in Fig. 1(a). The fabrication starts from a 300 µm thick glass substrate. First the sample is cleaned in hot piranha, followed by a hot acetone and isopropylalcohol clean and a 10 minutes oxygen plasma clean. By DC sputtering, 2 nm silver/ 100 nm gold/ 4 nm silver is deposited as bottom layer of the metallic slot waveguide. In this layer the 200 nm wide SPP excitation slit is defined by e-beam lithography and Xenon etching. The insulating layer exists out of a 100 nm thick oxygen plasma cured HSQ planarization layer. In this layer the Bragg mirror is defined by e-beam lithography and Xenon etching. The gratings are etched 13 to 52 nm deep inside the oxide with various pitches. The top metal layer is again deposited by sputtering and consists out of 4 nm silver/ 160 nm gold. In order to analyze the spectrum of the transmitted SPPs through the filter, in a similar way a 200 nm wide detection slit is etched in the top metal layer. So the idea is to excite SPPs by focusing white light from the coherent white light source on the excitation slit, the generated SPPs are transmitted/reflected by the filter and the resulting transmission spectrum is measured by spectroscopy. A top-view scanning electron micrograph of the Bragg filter can be found in Fig. 1(c). The injection slit, detection slit and filter are indicated with respectively I, D and F. The injection slit is barely visible due to the excellent planarization of the HSQ layer. In Fig. 1(d) a zoom-in on the filter region and injection slit is presented before the deposition of the top gold layer, conveying the quality of the device.

#156822 - $15.00 USD Received 19 Oct 2011; revised 2 Dec 2011; accepted 2 Dec 2011; published 30 Jan 2012

2.3. Optical transmission setup

The experimental investigation of the integrated Bragg filters requires the combination of local optical excitation of SPP's at one side of the sample and spectroscopy of outcoupled SPPs at the other side of the sample. A schematic overview of the setup is given in Fig. 1(b). White light from a fiber-coupled coherent white light source (5W Fianium) was used for plasmon excitation. The optical power of the laser is attenuated by two polarizers (P) and a neutral density filter wheel (A). The power on the sample after attenuation was varied between 0.1 mW and 10 mW, depending on the transmission efficiency of the device under study. The laser light is focused on the sample by means of a custom built microscope (M1) equipped with 100X/0.5NA NIR long working distance objective and CCD camera, allowing us to focus the laser spot on the 300 nm wide excitation slit. The sample (S) itself is mounted on a stage of which the position is controlled by both a mechanical and piezo translation stage. The light generation at the detection slit due to the transmitted SPPs which couple back out to free space light is collected by a second objective (20X/0.35NA VIS) mounted on a second microscope (M2). The light collected by this objective is then focused on the entrance slit of an imaging spectrometer by a tube lens (L) with a focal distance of 30 cm. One disadvantage of this optical setup is that only a cooled silicon CCD camera is available to perform spectral measurements, restricting the detectable wavelength range to 1050 nm.

2.4. Experimental waveguide characterization

In order to characterize the properties of surface plasmon propagation through the waveguide, we will use the SPP interference caused by two slits. By comparing the interference pattern for different distances with the simulated transmission spectra, we are able to find the surface plasmon polariton wave vector for excitation energies between 1.3 and 1.9 eV. In this way we can compose the surface plasmon dispersion relationship of MIM-SPPs and the effective index of the waveguide based on experimentally obtained transmission spectra. To accomplish this, the transmission spectrum of a MIM waveguide with injection and detection slit is measured under white light excitation. This is performed for injection-detection distances from 0 up to 7 micrometer in steps of 175 nm. In order to remove the spectral features originating from the white light source and other optical components in the optical path, all spectra are divided by a reference spectrum, for which we take the zero micrometer injection-detection distance spectrum. Resulting graphs for distances between 525 nm (the bottom black curve) and 3500 nm (the top gray curve) in steps of 175 nm are shown in Fig. 2(a). This range was chosen because the SPP interference can easily be measured as long as the distance between the two slits is lower than the SPP propagation distance. There is a clearly defined dependence of the normalized transmission spectrum on the length of the resonant cavity. By simulating the transmitted power through the waveguide by a FEFD solver (Comsol multiphysics [19]), we can compare the interference spectrum to the experimentally obtained transmission spectra for the different injection-detection distances. Since we fabricate our structures with a length of 30 micrometers in order to avoid edge effects, 2D simulations can be performed. In both FEFD and FDTD simulations, we program the geometry of the waveguide-integrated resonators and insert materials by means of the experimentally measured (n,k) values or known optical constants. For the glass substrate, we use the SiO_2 optical properties from Palik [20]. Perfectly matched layers were used as boundary condition. Insertion of the plasmonic guided mode was done by dipole excitation. Detection of the transmitted power through the filter was accomplished by positioning a power monitor behind the SPP filter. The only parameters that can be varied are the index (n=1.42) and thickness of the HSQ resist (100 nm), since they can vary slightly depending on the curing conditions. The optical properties of the gold are determined by ellipsometry measurements. The best correspondence with the experiments was found with a HSQ thickness

#156822 - $15.00 USD Received 19 Oct 2011; revised 2 Dec 2011; accepted 2 Dec 2011; published 30 Jan 2012

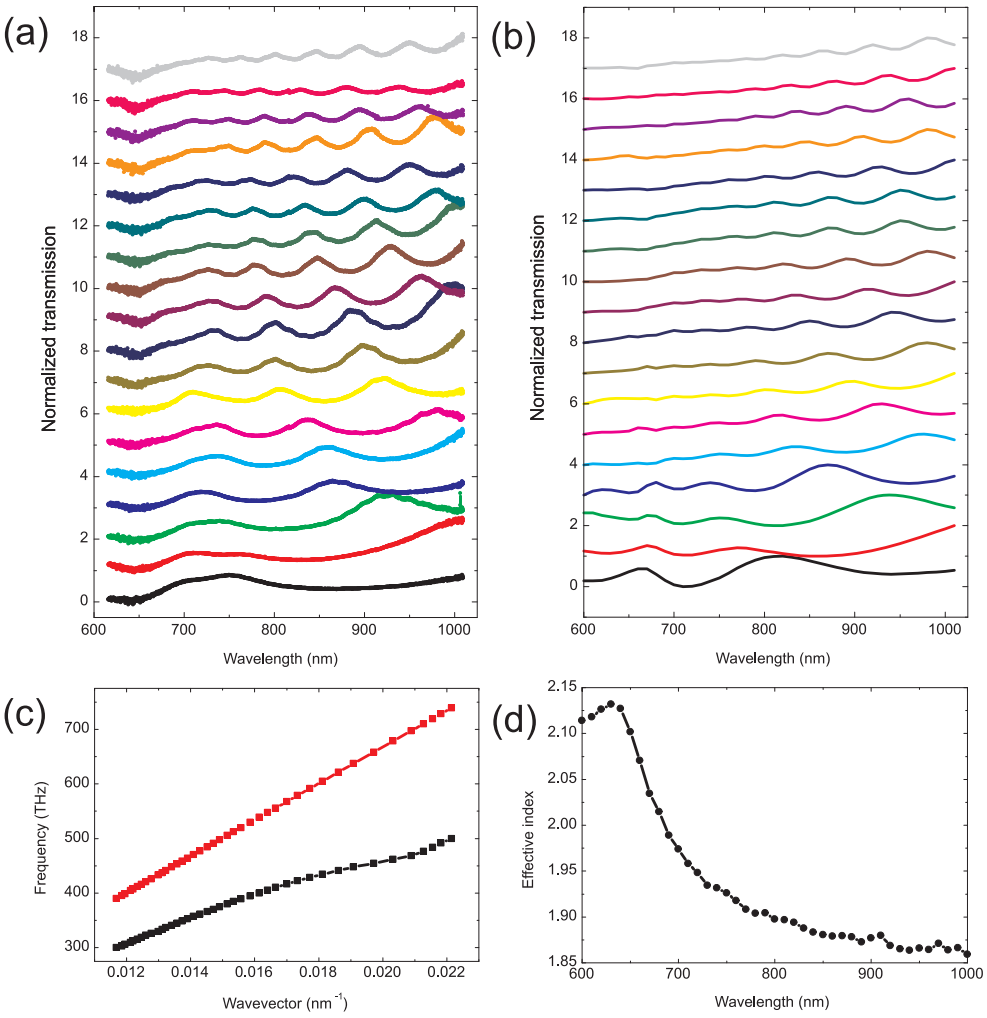

Fig. 2. **(a)** Experimental transmission spectra through a MIM waveguide for different distances between injection and detection slit, ranging from 525 (black) to 3500 nm (gray). **(b)** Simulated transmission spectra for the same geometrical and optical parameters as in the experiment. **(c)** Calculated dispersion curve (black line) based on the fitting of the experimental results together with the light line in the dielectric (red line). **(d)** Effective index of the MIM waveguide.

#156822 - $15.00 USD Received 19 Oct 2011; revised 2 Dec 2011; accepted 2 Dec 2011; published 30 Jan 2012

of 98 nm and an index of 1.44. The resulting simulated SPP transmission curves are shown in Fig. 2(b). Once a good correspondence between simulation and experiment is obtained, the plasmon wavelength can be determined for each wavelength point in the simulation. In Fig. 2(c), the dispersion relationship of waveguided slot plasmons is shown by the black curve, together with the dispersion curve of light in the dielectric medium. It can be noticed that due to the interband transitions inside the gold layers that cause high losses for the highest energies, the dispersion curve starts to bend back towards the light line. The dispersion relation can also be expressed in terms of the effective index of the guided mode. This is displayed in Fig. 2(d). As the mode index increases for decreasing oxide thickness in MIM waveguides and we use a relatively thick oxide, we obtain a maximum index of 2.13 for a free space wavelength of 630 nm. For longer wavelengths, the effective index is lower due to a lower confinement, as could be observed in the found dispersion curve. For wavelengths shorter than 630 nm, strongly increased losses prevent higher confinement of the plasmonic mode.

2.5. Characterization of the integrated Bragg filters

To predict the properties of the proposed filters, FDTD simulations are carried out. In literature, the effect of periodic gratings on propagating surface plasmon polaritons has been studied theoretically [14, 15, 21, 22] and experimentally [23, 24] in several geometries. Although similar simulations on Bragg gratings are already performed in literature, the characterization of the Bragg filters is important for two reasons. First we have to find the optimal processing parameters to design the Bragg mirrors in the desired wavelength region with the preferred width of the stop-band in order to successfully obtain experimental results on the Bragg filters. Second, in the next section the Bragg filters are applied for the design of plasmonic crystal resonators, for which it is crucial to assess the properties of the Bragg reflectors. A schematic picture of the Bragg mirror inside the MIM waveguide together with the different parameters is presented in 3a.

Formula 1 shows us that we can easily tune the center wavelength of the Bragg reflector by changing d_1 and d_2. In our design, we will keep these two distances equal to each other. As a consequence, the center wavelength of the stop-band is determined by the pitch of the grating and the effective indices. In the FDTD simulations, surface plasmon polaritons are generated by dipole excitation inside the waveguide. By monitoring the transmitted SPP power after the integrated filter and dividing by the reference spectrum (for which we take the transmitted power without the presence of the filter), the spectral characteristics of the filter can be acquired. In order to very clearly visualize the effect of the geometrical parameters of the device on the transmission of the Bragg filters, we will show the optical transmission spectra over the entire VIS-NIR spectral regime, although experiments could only be performed for wavelengths below 1050 nm. In Fig. 3(b), the normalized transmitted power through the filter is obtained for a Bragg reflector with 8 periods and an etch depth of 30 nm. The transmission spectrum is shown for a pitch of 260, 320 and 380 nm, confirming that by altering the pitch, the Bragg wavelength can be tuned easily over the VIS-NIR spectrum.

In order to adjust the width of the stop-band, Eq. (2) tells us that we have to change the difference between the effective indices inside the filter. One way to achieve this is to locally vary the refractive index of the dielectric layer of the guide [14] or the index of the metals [25]. Although this method gives good results in numerical calculations, the alteration in refractive index is quite hard to realize in practice. Therefore, as one could already see in the presented design, an easier and more appropriate way of obtaining an effective index difference inside the SPP waveguide is to locally change the thickness of the waveguide by introducing a gold grating structure in the waveguide. In Fig. 3(c), this is clearly demonstrated. The transmission spectrum is shown for a Bragg grating with 8 periods and a pitch of 320 nm. The etching depth

#156822 - $15.00 USD Received 19 Oct 2011; revised 2 Dec 2011; accepted 2 Dec 2011; published 30 Jan 2012

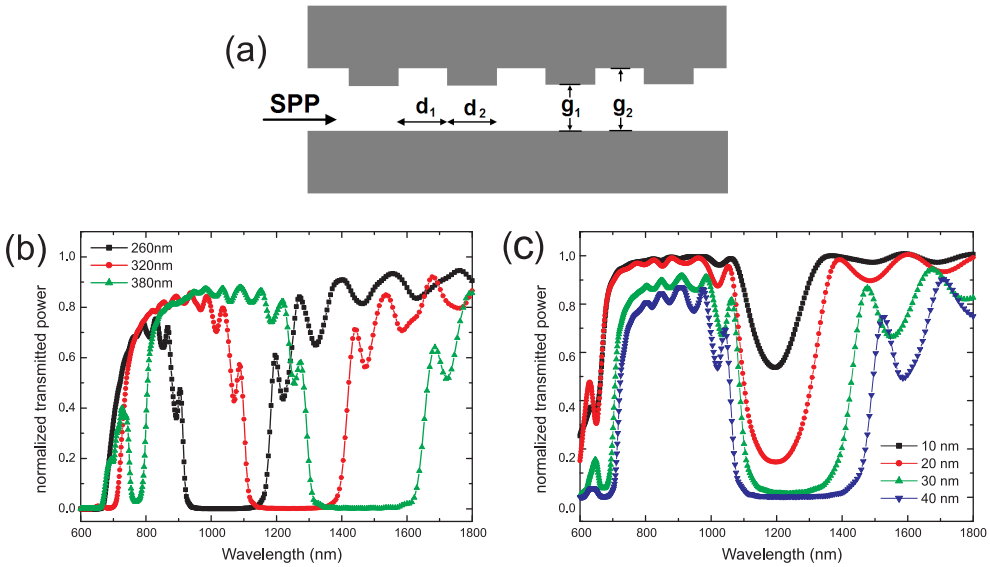

Fig. 3. **(a)** Schematic overview of the integrated Bragg reflector. d_1 and d_2 define the grating's pitch and g_1 and g_2 define the etch depth of the grating. **(b)** Numerical simulations of the SPP transmitted power through the Bragg filter for different pitches of the grating. **(c)** Numerical simulations of the SPP transmitted power through the Bragg filter for different etching depths.

in the insulator is varied from 10 to 40 nm (g_2 = 100 nm, g_1 varies from 90 to 60 nm), revealing the dependence of the stop-band width on the etch depth, and thus on the effective index contrast. When a low index contrast is used, the reflected SPP intensity of the filter for wavelengths inside the stop-band is quite low, as can clearly be noticed in the graph when a etch depth of 10 nm is used. As the depth increases and subsequently the index contrast increases, the Bragg mirrors become more efficient and a lower SPP transmission is observed. By increasing the index difference, not only the width of the band increases, but also the attenuation within the band increases significantly. However, it should be pointed out that using a large etching depth also leads to a drop in the band-pass transmission efficiency.

First we to assess the spectral position and width of the reflector stop-band. For the gratings, three parameters of the gratings were varied in e-beam mask design: the grating pitch, the etching depth and the number of grating periods. The pitch was varied from 200 to 450 nm in steps of 25 nm, gratings with etch depths of 13, 26, 39 and 52 nm were fabricated and the number of periods varied from 6 to 12 in steps of 2. The distance between the injection slit and the grating was kept constant for all devices at a distance of 1 micrometer. The length of the slits and gratings was chosen to be as large as 30 micrometer, to ensure no edge effects would manifest during the optical measurements.

As could be seen in Fig. 3(b), the width of the stop-band is strongly dependent on the etching depth. Because of this, for larger etching depths only the left side of the stop-band or even no band is observed for most fabricated Bragg mirrors due to the limited detection range of the silicon CCD camera. The gratings with pitches ranging from 200 up to 450 nm lead to a stop-band center of respectively 820 nm up to 2 μm. Using a 200 nm wide subwavelength slit, plasmons are optically excited from the top of the sample, and the response of the filter is picked up at the detection slit through the glass substrate. In first instance, we will study the Bragg reflector

#156822 - $15.00 USD Received 19 Oct 2011; revised 2 Dec 2011; accepted 2 Dec 2011; published 30 Jan 2012

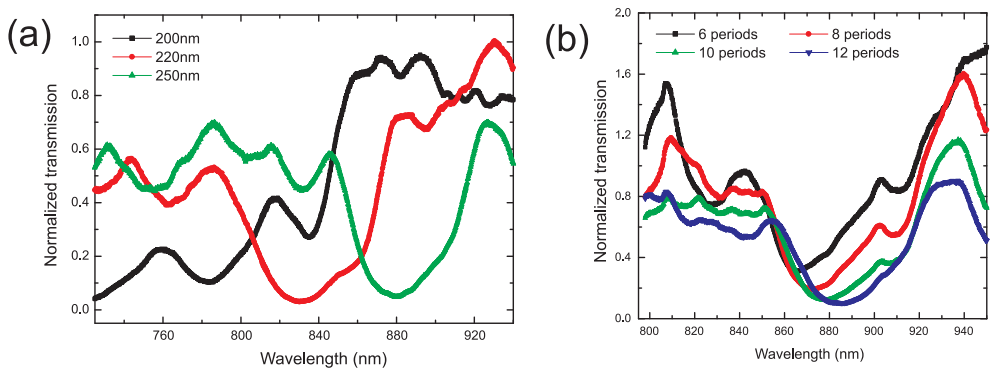

Fig. 4. **(a)** Experimental measurement of the normalized transmission spectrum of 13 nm deep Bragg gratings with 12 periods for different pitches (200,220 and 250 nm). **(b)** Experimental measurement of the transmission spectrum of a 13 nm deep Bragg grating with a pitch of 250 nm for grating periods of 6, 8, 10 and 12.

characteristics as a function of the pitch of the grating. In Fig. 4(a), the experimental normalized transmitted light spectrum is plotted for three different pitches (200, 220 and 250 nm) for a filter with 13 nm etching depth and 12 grating periods. First the background spectrum (spectrum measured without white light excitation) is subtracted from the transmission measurements. The resulting spectrum is consequently normalized to the measured transmission through an open window in order to remove the spectral features of the laser and other components in the optical beam path. The resulting graph shows a clear shift to longer wavelengths of the center of the stop-band for an increasing grating period. The width of the optical band gap is quite low due to the low effective index difference between the etched and not-etched parts of the grating, leading to a relatively high SPP transmission inside the optical stop-band.

In the measurement range, it was difficult to measure the effect of the etching depth on the shape, efficiency and spectral position of the optical bandgap. Another method to evaluate the decrease in SPP transmission through the Bragg mirror inside the stop-band consists of varying the number of periods in the grating reflector. In Fig. 4(b), the background-subtracted transmission spectrum of an integrated Bragg reflector with 250 nm pitch and 13 nm etching depth is shown for four different numbers of periods. For the largest number of periods, one can observe that the SPP transmission in the stop-band is the lowest. However also the SPP transmission for wavelengths outside the stop-band spectral range are attenuated more when the efficiency of the Bragg mirrors is increased, which is clearly visible in the graph. Furthermore the expected widening of the band is observed in for an increasing number of periods.

3. Transmission filters by integrated plasmonic crystal resonators

3.1. Fabrication of waveguide-integrated resonant cavities

For the integrated resonators, the same fabrication procedure was used as for the Bragg filters. Only in the second e-beam step, where the gratings are defined, the nanocavity is introduced in the middle of the Bragg grating. After fabrication the cavities are first observed by scanning electron microscopy. A top-view nanocavity SEM photograph of a plasmonic crystal resonator is shown in Fig. 1(c). The two slits marked by the capital D are two output slits, both positioned at the same distance from the SPP input slit (I). Between the injection slit and the top output slit the filter (F) is processed. A clearer picture of the filter before gold deposition of the top gold

#156822 - $15.00 USD Received 19 Oct 2011; revised 2 Dec 2011; accepted 2 Dec 2011; published 30 Jan 2012

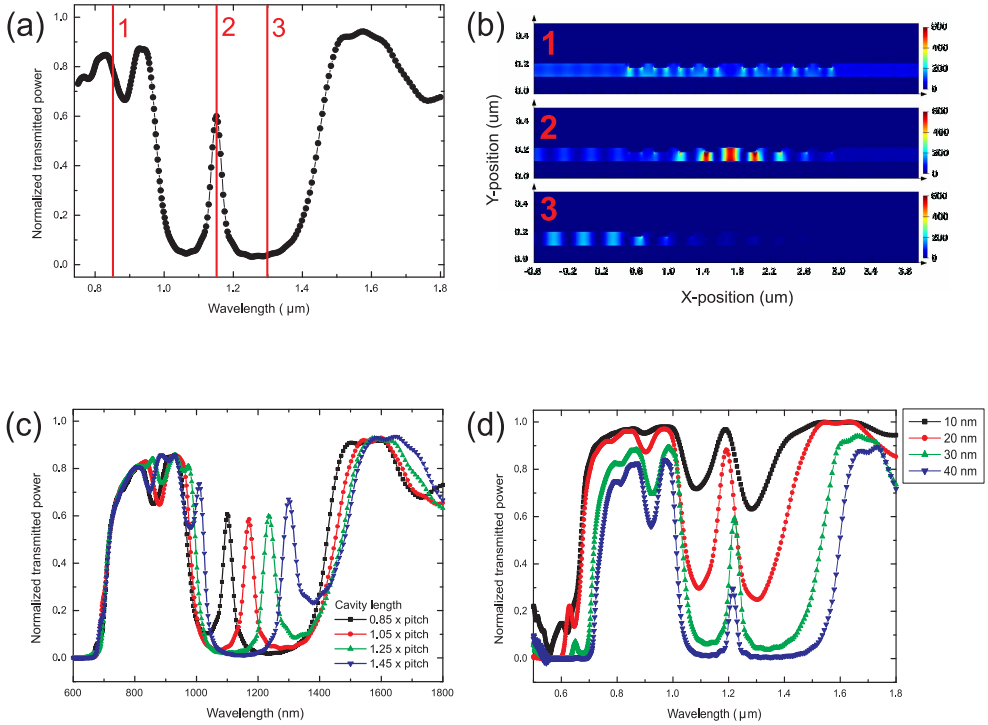

Fig. 5. Simulation of the plasmonic crystal resonator. **(a)** Normalized transmission spectrum of a plasmonic crystal resonator with Bragg reflectors with 4 periods of 300 nm at each side of the nanocavity, which has a length of 300 nm. As reference for normalization, the transmitted power spectrum is chosen in the case where no filter is present. **(b)** The normalized electric field profile is given for the three lines indicated in a). The first on is outside the stop-band, the second on the resonance and the third in the stop-band, but off-resonance. **(c)** Normalized transmission spectrum for a plasmonic crystal with 300 nm pitch for cavity lengths of respectively 0.85, 1.05, 1.25 and 1.45 times the pitch. Changing the cavity length clearly allows tuning of the resonant wavelength. **(d)** The normalized transmitted power of the plasmonic crystal for different etching depths.

layer is shown in Fig. 1(d).

3.2. Simulated transmission spectra of plasmonic crystal filters

By introducing a defect inside the Bragg reflector, one can create a resonant nanocavity. Depending on the length of the defect compared to the pitch of the Bragg grating, the resonance wavelength of the cavity can be positioned in the middle of the stop-band of the reflector, leading to a very strong resonance with high quality factor. For the reflectors, a perfect symmetric Bragg grating was used at both sides of the defect. A schematic representation of the structure can be found in Fig. 1(a). From simulations it follows that these slits introduce extra interference peaks outside the optical bandgap, but inside the band, the filter characteristics strongly dominate the transmission spectrum. Similar to the previous section, we excite the SPPs inside the waveguide by dipole excitation and monitor the transmitted power spectrum behind the filter.

From the previous section we already know how to vary the optical properties of the Bragg

#156822 - $15.00 USD Received 19 Oct 2011; revised 2 Dec 2011; accepted 2 Dec 2011; published 30 Jan 2012

reflectors all over the VIS-NIR spectral range. For an etching depth of 30 nm, we varied the length of the defect and found that we can tune the resonance wavelength inside the stop-band. Of course these values are strongly dependent on the etch depth of the reflector. In Fig. 5(a), the simulated normalized transmitted power is shown for a plasmonic crystal filter with Bragg reflectors with four periods of 300 nm at each side of the defect, which has a 300 nm length. A resonance with quality factor of 25.5 and a normalized transmission of 60 percent is observed inside the stop-band. In Fig. 5(b) the normalized electric field profile is given for three different wavelengths as shown by the red lines in Fig. 5(a). When the cross-section field profile is calculated outside the stop-band (line 1), one can see that most of the power is transmitted through the filter. Almost no interference between incident and reflected SPPs is observed. When taking a look at the electric field profile at the resonance wavelength (line 2), a strongly confined mode with a strongly enhanced electric field around the defect is observed. While a small part of the SPP power is reflected due to the Bragg reflector, leading to a faint interference pattern in the beginning of the waveguide, most of the power is transferred to the resonant cavity, leading to a 60 percent transmission of the filter at the resonance wavelength. When the electric field profile is calculated inside the stop-band but off-resonance (line 3), one can see that all power is reflected due to the Bragg reflector, causing a strong interference pattern in front of the filter.

The resonance center wavelength can easily be tuned by varying the length of the defect cavity. In Fig. 5(c), the normalized transmission spectrum for a plasmonic crystal resonator with 300 nm pitch and 30 nm etch depth is displayed for cavity lengths of 0.85, 1.05, 1.25 and 1.45 times the pitch. It can be seen that the main resonant mode can be shifted throughout the entire optical bandgap by changing the cavity length. The quality factor of the resonance can be tuned by changing the efficiency of the reflectors. As a consequence, a higher Q-factor is obtained by increasing the number of grating periods or increasing the refractive index difference inside each period achieved by a deeper grating etch. An example of this can be found in the graph in Fig. 5(d), where the normalized transmitted power spectrum is given for four different etching depths for the same plasmonic crystal filter as in Fig. 5(a). Due to the higher reflectivity of the mirrors for a deeper gold etch, etching 10, 20, 30 and 40 nm deep gratings inside the gold results in a quality factor of respectively 13, 18, 26 and 41. However, next to a stronger resonance, this higher reflector efficiency causes also a drop in transmission (respectively 95, 88, 60 and 30 percent) at the resonance wavelength.

3.3. Experimental results of plasmonic crystal filters

The measurements in this paragraph are performed on a resonator based on a Bragg grating with an etch depth of 26 nm and a pitch of 200 nm. The reason for this choice is that the bandgap lies in the detectable range of the CCD camera and the experimentally observed resonant mode completely falls inside the optical bandgap. For the devices with 13 nm etching depth, the modal shift of the cavity resonance could also be observed, but due to the spectrally broader resonance and the smaller stop-band, the mode always overlaps with the edges of the stop-band, thereby making it difficult to characterize the properties of the resonance. When going to larger etching depths (39 and 52 nm), transmission through the filter was too low to observe the characteristics of the fabricated filters and resonators.

In Fig. 6(a) and 6(b), the measured and simulated transmission spectrum of two resonators with cavity lengths of 150 and 220 nm are shown together with the transmission spectrum of the Bragg grating without defect structure, serving as a reference. The measured spectra were divided by a reference spectrum, for which we take the transmission spectrum for the MIM waveguide with two 300 nm wide slits on top of each other. A first comparison between the measured and calculated spectra shows us that while the left edge of the stop-band is clearly present in the simulations, the experiments only have a very weakly pronounced edge around

#156822 - $15.00 USD Received 19 Oct 2011; revised 2 Dec 2011; accepted 2 Dec 2011; published 30 Jan 2012

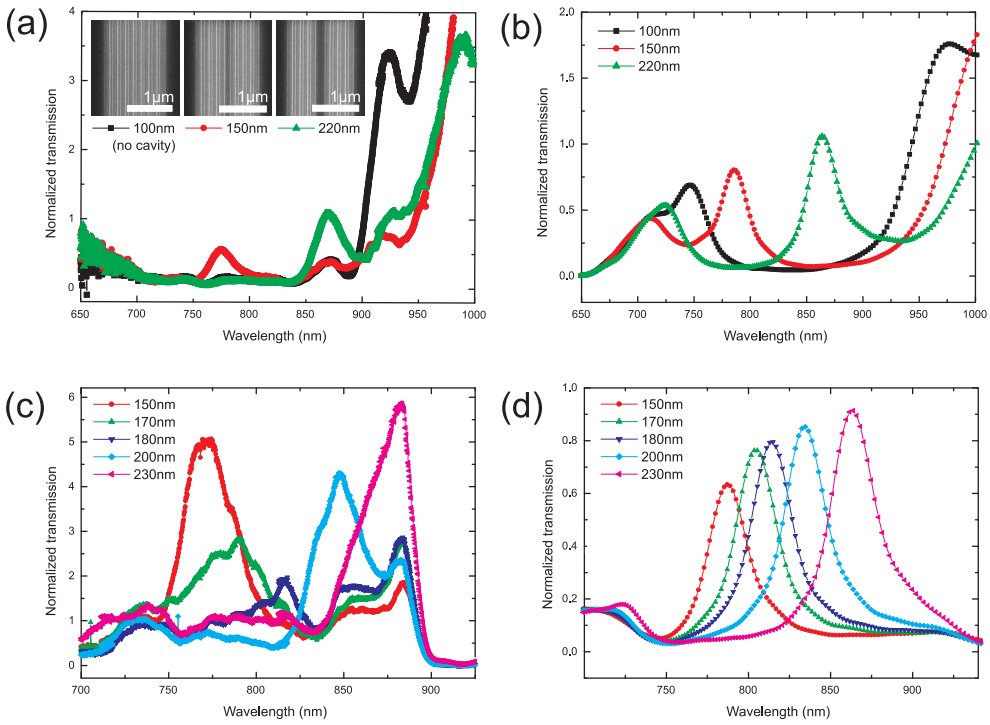

Fig. 6. **(a)** Transmission spectrum of two resonant cavities of 150 and 220 nm width inside a Bragg grating with a pitch of 200 nm. As a reference also the transmission of the grating without cavity is plotted. SEM pictures corresponding to the measured devices are shown in the inset. The high-Q resonance appears inside the bandgap (750-870 nm). **(b)** Simulated transmission spectrum for the two geometries used in a. **(c)** Transmission spectrum divided by the reference spectrum, showing the dependence of the resonant mode on the cavity length. **(d)** Simulated transmission spectrum for the same device geometries as in figure c.

750 nm. Below a free space wavelength of 700 nm, the high losses inside the metal parts of the waveguide cause the signal to fall within the noise level for all devices, as can be seen in Fig. 6(a). The low-energy edge of the optical bandgap is very clearly visible and lies just below a wavelength of 900 nm (black curve). When introducing a 150 nm wide defect cavity in the middle of the 200 nm pitch Bragg grating, a resonant mode is created with a resonant wavelength close to the high-energy edge of the optical bandgap, as is shown by the red curves in Fig. 6(a) and Fig. 6(b). The quality-factor of the resonance at a wavelength of 775 nm is determined to be 31, compared to 33 in the simulation. Although there is no huge difference in the quality factor, the transmission at the resonance frequency is found to be much lower than the transmitted light outside the bandgap, in contradiction to the simulations, where the transmitted power is over 70 percent of the transmitted power without filter. The resonance can be tuned by changing the length of the cavity. By changing the cavity from 150 nm to a length of 220 nm, the resonance is shifted through the entire optical band gap from 775 to 870 nm. To investigate the evolution of the resonant mode inside the stop-band, transmission measurements were performed with varying cavity lengths. The experimental results are presented in Fig. 6(c) and the corresponding simulations can be seen in Fig. 6(d). To observe the modes inside the bandgap better, we normalized the transmitted spectra by the spectrum of the Bragg filter

#156822 - $15.00 USD Received 19 Oct 2011; revised 2 Dec 2011; accepted 2 Dec 2011; published 30 Jan 2012

without cavity. The shift of the mode to longer wavelengths with increasing cavity lengths can clearly be observed in the measurements and correspond well to the spectral positions of the simulated resonant plasmon modes. Experimentally, the transmission of the mode is the most attenuated in the middle of the optical bandgap, where the SPP reflection is highest. However in the numerically obtained spectra, no attenuation of the mode is observed in this particular configuration when the mode is varied throughout the optical bandgap. When the efficiency of the reflector is increased, either by a deeper grating etch or a higher number of periods, a small decrease of the transmission efficiency of mid-gap modes compared to edge-gap modes is observed. However no good explanation is found for the strong attenuation of the resonant mode as found in the presented experimental results.

4. Metallic reflector transmission filters

In this paragraph we will numerically show that a waveguide-integrated cavity structure can not only be realized by changing the dielectric index or the modal index of the waveguide, but also can be achieved by incorporating metallic reflectors inside the waveguide. In this way we remove the necessity of micron-size Bragg gratings, making this a resonator on the nano-scale in three dimensions. Due to its small dimensions compared to the plasmonic crystal resonators, also losses due to resistive heating are strongly reduced, leading to a higher transmitted power at resonance.

In Fig. 7(a), a schematic representation of the structure under study is given. Again the standard gold-SiO_2-gold MIM waveguide is used with a insulator core thickness of 100 nm. The cavity structure is formed by two vertical gold barriers. In practice, this structure could be fabricated by focused ion beam milling inside the insulator layer, followed by gold evaporation or electroplating of the top metal layer. Due to partial optical transmission and reflection occurring at the two thin gold barriers, a resonance is formed when

$$2L_{cav}k_{SPP} + 2\phi = 2\pi n \tag{3}$$

with L_{cav} the cavity length, k_{SPP} the SPP wave vector, ϕ a phase shift upon reflection and n an integer number. For off-resonance wavelengths, no efficient resonant coupling to the cavity is possible and as a consequence the transmission is very low since the two metal barriers are highly reflective. This is a great advantage compared to the plasmonic crystal cavities, since the transmission for off-resonant wavelengths is very low over the entire spectrum, while for plasmonic crystal cavities the spectral range of the zero-transmission region only has a limited spectral range determined by the stop-band of the Bragg gratings.

In order to study the spectral transmission through the cavity filter, 2 dimensional FDTD simulations were performed. SPP generation inside the waveguide was achieved by dipole excitation. The transmitted power after the filter is monitored. In order to get an absolute value for the transmission through the filter, the SPP decay inside the waveguide has to be accounted for. Therefore the power spectrum after the filter is normalized to the power spectrum for the case where no filter is present. The normalized transmission spectrum of a 500 nm wide cavity with 20 nm wide metal reflectors is shown in the top panel of Fig. 7(b). For this width, we can observe that the three first resonant modes (n=1,2,3) fit in the cavity for free space wavelengths between 500 and 2200 nm. In the bottom panel of Fig. 7(b) the normalized electric field profile inside the cavity is shown for the different wavelengths indicated by the red lines in the transmission spectrum. For the resonant wavelengths (line 1, 2 and 3), clearly 1, 2 and 3 nodes are found inside the cavity, and SPP transmission is observed after the cavity. In the fourth normalized E-field profile, corresponding with line 4 in the transmission spectrum, the normalized electric field profile for an off-resonant wavelength of 1.15 μm is shown. No SPP transmission is observed in this case as only a strong reflection is observed at the first and second gold bar-

#156822 - $15.00 USD Received 19 Oct 2011; revised 2 Dec 2011; accepted 2 Dec 2011; published 30 Jan 2012

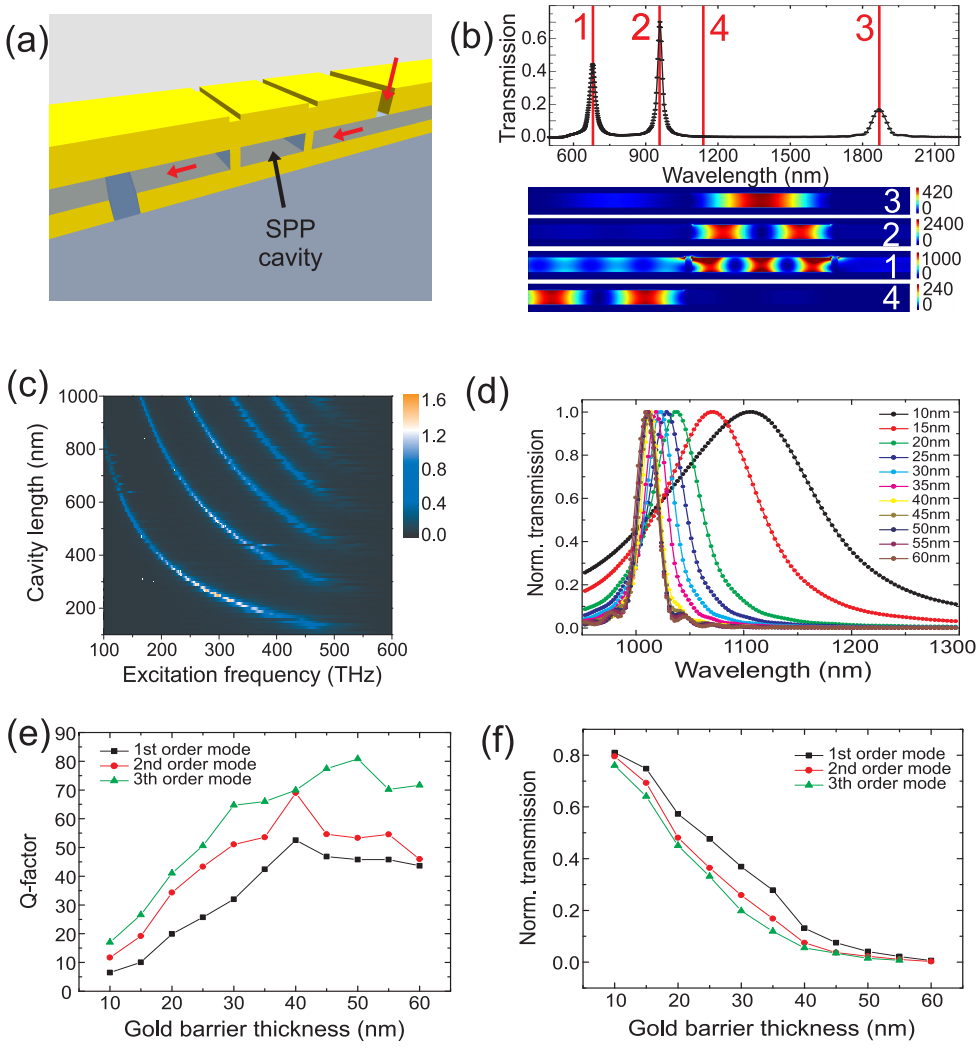

Fig. 7. **(a)** Schematic picture of the metallic reflector resonator filter. **(b)** Normalized transmitted power for a 500 nm long cavity together with the normalized electric field profiles. **(c)** Colorplot of the transmitted power through the filter as a function of the excitation frequency and the cavity length. **(d)** Transmitted power normalized to the peak value as a function of the gold barrier thickness. **(e)** Quality factor for the three lowest order modes as a function of the barrier width. **(f)** Normalized transmitted power for the three lowest order modes as a function of the barrier width.

#156822 - $15.00 USD Received 19 Oct 2011; revised 2 Dec 2011; accepted 2 Dec 2011; published 30 Jan 2012

rier.

The principles of tuning the resonant wavelength of the integrated metallic reflector resonator is similar to the plasmonic crystal waveguide resonator. The method of shifting the center wavelength of the resonance is determined by the resonance condition defined in Eq. (3). As is the case for plasmonic crystal resonators and many other resonators, the spectral position of the resonance can be altered by changing the cavity length. Figure 7(c) depicts a color plot of the transmitted power through the filter as a function of the excitation frequency and the cavity length. A standard Fabry-Perot mode plot is obtained. The spectral region where interband transitions lead to increased losses in the cladding layers can clearly be seen at the right of the plot. The lowest order mode (n=1) appears for a cavity length of 150 nm. For increasing cavity lengths, higher order resonant modes appear in the spectral transmission. The predicted spectral shift as a function of the cavity length is clearly observed. A sharp resonance that is indicative of a high quality-factor mode is observable for all nanocavities. The quality factor for the nanocavity resonances is mainly determined by the intrinsic metallic losses from both the waveguide cladding layers and the metallic mirrors. From the colorplot, it can already be noticed that for the same excitation frequency, the quality factor for the second order mode is higher than the first order mode. In order to investigate the quality factor, we can study the effect of changing the efficiency of the two gold barrier reflectors on the quality factor. The reflectivity from and transmission through the gold barriers can easily be changed by altering their thickness. In Fig. 7(d) the transmission through a 250 nm long cavity resonator is calculated for the first order mode. The thickness of the gold barrier reflectors is varied from 10 to 60 nm. Since the transmitted power through the resonator varies over several orders of magnitude for the different reflector widths, the transmission spectrum is normalized to the peak value. With an increase in barrier thickness and hence an increasing reflector efficiency, a stronger resonance is obtained and as a result a narrowing of the spectral width is observed. The resulting Q-factors for the n = 1, 2 and 3 is plotted in Fig. 7(e) as a function of the barrier thickness. The width of the cavities is taken to be respectively 250, 500 and 700 nm in order to have the resonant wavelength for the three modes around a value of 1000 nm. The quality factor is found to be an increasing function of the barrier thickness. However if the barrier thickness becomes too large, the reflection becomes to large to efficiently couple in from the propagating plasmon mode to the resonant cavity. Therefore above a thickness of 40 nm, the quality factor saturates and eventually decreases. Of course this effect manifests itself in the transmitted power through the filter, which is depicted in Fig. 7(f), again for the three lowest modes. As the reflector thickness increases, the Q-factor increases but due to a lower incoupling efficiency, the transmission through the filter decreases. Above 40 nm, almost no power is transmitted through the resonant cavity. Although the simulations presented in this section are 2-dimensional FDTD simulations, 3-dimensional simulations prove that this type of resonator can also be applied in waveguides with subwavelength lateral dimensions.

The important parameters characterizing the waveguide-integrated resonators are the size, quality factor and transmission efficiency. In literature, many waveguide-integrated resonators were proposed and studied theoretically or numerically. However only few were realized experimentally. Higher resonators have been shown (e.g. a SPP whispering galery resonator with a Q of 1376 [26]). The high Q goes together, however, with a relatively large size, little confinement and difficult waveguide integration. Also ring resonators with a radius of 5 microns in plasmonic groove waveguides were realized [23] in order to filter one specific wavelength range. Other research groups proposed a waveguide-integrated resonator by introducing one or more vertical cavities inside the waveguide, both for MIM (predicted Q between 30 and 40 [27]) and flat waveguides (demonstrated Q of 45 [28]. Many other resonators were proposed and studied by simulations, e. g. racetrack resonators [29,30], nanodisk resonators [31] and ver-

#156822 - $15.00 USD Received 19 Oct 2011; revised 2 Dec 2011; accepted 2 Dec 2011; published 30 Jan 2012

tical cavity resonators [32,33]. Our resonant cavities have the particular advantage that they can be integrated inside nanoscale, high-confinement plasmonic waveguides. Quality factors of our devices were similar to the previously discussed waveguide-integrated resonators, but the size can be made considerably smaller, certainly in case of the metallic reflector resonators. However, for this type of high-confinement waveguide resonators, there will always be a trade-off between the quality factor and the transmission efficiency at resonance.

5. Conclusion and discussion

We can conclude that we were able to design, simulate, process and measure transmission filters and resonators based on waveguide-integrated Bragg gratings. Integrated band-stop filters were developed with varying reflection efficiencies and band-center wavelengths. By introducing a cavity inside the grating, a resonant mode inside the stop-band was observed with a relatively high Q-factor of 31. In the future, a full set of measurements should be obtained by extending spectral range the optical setup into the infrared region. For the smallest Bragg periods which were used in the presented measurements, structural imperfections (with spatial dimensions similar to the period length) play an important role in the generation of extra losses inside the gratings. This may lead to a decrease in quality factor and transmission of the resonant mode. When switching to longer Bragg periods and cavity lengths, and thus longer wavelengths, the influence of these defects will decrease, leading to an improved performance of the filters and resonators. Also the SPP propagation distance is significantly longer at infrared wavelengths, increasing the strength of the resonant mode compared to the 600-1050 nm range we are working in now. Metallic reflector resonators were proposed as a waveguide-integrated resonator with nanoscale size in three dimensions. A waveguide-integrated transmission filter based on an integrated Fabry-Perot resonator was designed by introducing two gold barriers in a MIM waveguide. The strength of the resonances could be tuned by altering the metallic reflector thicknesses, leading to quality factors up to 80. Not only can these structures be used for fabricating integrated filters, they also provide an ideal platform for future nanoscale waveguide-integrated electrically pumped lasers.

#156822 - $15.00 USD Received 19 Oct 2011; revised 2 Dec 2011; accepted 2 Dec 2011; published 30 Jan 2012